2019

Modulation of terahertz radiation from graphene surface plasmon polaritons via surface acoustic wave

Sichen Jin
Capital Normal University

Xinke Wang
Capital Normal University

Peng Han
Capital Normal University

Wenfeng Sun
Capital Normal University

Shengfei Feng
Capital Normal University

See next page for additional authors

Modulation of terahertz radiation from graphene surface plasmon polaritons via surface acoustic wave

Abstract

We present a theoretical study of terahertz (THz) radiation induced by surface plasmon polaritons (SPPs) on a graphene layer under modulation by a surface acoustic wave (SAW). In our gedanken experiment, SPPs are excited by an electron beam moving on a graphene layer situated on a piezoelectric MoS 2 flake. Under modulation by the SAW field, charge carriers are periodically distributed over the MoS 2 flake, and this causes periodically distributed permittivity. The periodic permittivity structure of the MoS 2 flake folds the SPP dispersion curve back into the center of the first Brillouin zone, in a manner analogous to a crystal, leading to THz radiation emission with conservation of the wavevectors between the SPPs and the electromagnetic waves. Both the frequency and the intensity of the THz radiation are tuned by adjusting the chemical potential of the graphene layer, the MoS 2 flake doping density, and the wavelength and period of the external SAW field. A maximum energy conversion efficiency as high as ninety percent was obtained from our model calculations. These results indicate an opportunity to develop highly tunable and integratable THz sources based on graphene devices.

Disciplines

Engineering | Science and Technology Studies

Publication Details

Jin, S., Wang, X., Han, P., Sun, W., Feng, S., Ye, J., Zhang, C. & Zhang, Y. (2019). Modulation of terahertz radiation from graphene surface plasmon polaritons via surface acoustic wave. Optics Express, 27 (8), 11137-11151.

Authors

Sichen Jin, Xinke Wang, Peng Han, Wenfeng Sun, Shengfei Feng, Jiasheng Ye, C Zhang, and Yan Zhang

Research Article | Vol. 27, No. 8 | 15 Apr 2019 | OPTICS EXPRESS 11137
Optics EXPRESS

Modulation of terahertz radiation from graphene surface plasmon polaritons via surface acoustic wave

SICHEN JIN,[1] XINKE WANG,[1] PENG HAN,[1,3] WENFENG SUN,[1] SHENGFEI FENG,[1] JIASHENG YE,[1] CHAO ZHANG,[2] AND YAN ZHANG[1,4]

[1]*Department of Physics, Beijing Key Laboratory for Metamaterials and Devices, Key Laboratory of Terahertz Optoelectronics, Ministry of Education, Beijing Advanced Innovation Center for Imaging Theory and Technology, Capital Normal University, Beijing 100048, China*
[2]*School of Physics and Institute for Superconducting and Electronic Materials, University of Wollongong, New South Wales 2522, Australia*
[3]*hanpeng0523@163.com*
[4]*yzhang@mail.cnu.edu.cn*

Abstract: We present a theoretical study of terahertz (THz) radiation induced by surface plasmon polaritons (SPPs) on a graphene layer under modulation by a surface acoustic wave (SAW). In our *gedanken* experiment, SPPs are excited by an electron beam moving on a graphene layer situated on a piezoelectric MoS_2 flake. Under modulation by the SAW field, charge carriers are periodically distributed over the MoS_2 flake, and this causes periodically distributed permittivity. The periodic permittivity structure of the MoS_2 flake folds the SPP dispersion curve back into the center of the first Brillouin zone, in a manner analogous to a crystal, leading to THz radiation emission with conservation of the wavevectors between the SPPs and the electromagnetic waves. Both the frequency and the intensity of the THz radiation are tuned by adjusting the chemical potential of the graphene layer, the MoS_2 flake doping density, and the wavelength and period of the external SAW field. A maximum energy conversion efficiency as high as ninety percent was obtained from our model calculations. These results indicate an opportunity to develop highly tunable and integratable THz sources based on graphene devices.

1. Introduction

Terahertz (THz) radiation, which describes electromagnetic waves with frequencies in the 0.1–30 × 10^{12} Hz range, is one of the most important types of radiation for light sources in the fields of sensing and imaging because of promising properties that include low photon energy, broad spectral information, and high penetration of nonpolar materials [1]. At present, THz technology is widely used in fields including semiconductor science [2], noninvasive flaw detection [3], substance identification [4], and security inspection [5]. A THz radiation source with broad bandwidth, high intensity and frequency tunability is highly desirable. Several approaches, including photoconductive antennas [6], optical rectification [7], air plasmons [8], quantum cascade lasers [9], and free-electron beam excitation have been used to produce THz wave emission.

Among these approaches, free-electron THz radiation sources are of particular interest because of their high light radiation powers and continuously tunable radiation frequencies [10,11]. In contrast to traditional free-electron THz sources, in which a beam of electrons is accelerated to almost the speed of light c using an electron accelerator with large associated facilities requirements, excitation of THz radiation by a relatively low energy electron beam moving on top of graphene layers was recently proposed as a new THz source [11–16]. In this approach, surface plasmon polaritons (SPPs) with resonance frequencies in the 1–30 THz range are excited by a beam of moving electrons with speeds of less than 0.1c on top of graphene

#358815 https://doi.org/10.1364/OE.27.011137
Journal © 2019 Received 28 Jan 2019; revised 15 Mar 2019; accepted 17 Mar 2019; published 5 Apr 2019

Optics EXPRESS

layers. The energies of these resonant SPPs are then emitted into free space to radiate THz waves when the wavevectors of the SPPs and the electromagnetic wave are matched.

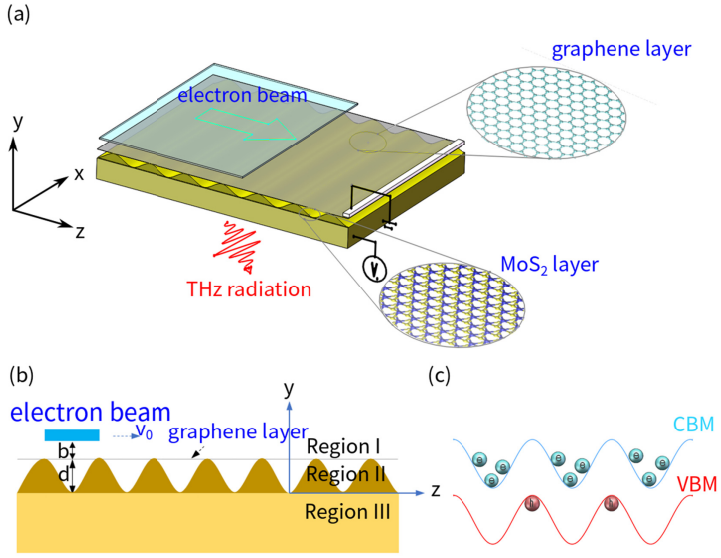

Fig. 1. (a) Three-dimensional and (b) side schematic views of a moving electron beam atop a graphene layer on a piezoelectric MoS_2 flake under an applied surface acoustic wave (SAW) field. The vacuum layer, the MoS_2 flake with the applied SAW field, and the substrate layer are labeled as regions I, II, and III, respectively. The distance between the electron beam and the graphene layer and the thickness of the MoS_2 flake are labeled b and d, respectively. (c) Schematic illustration of the electron and hole distributions in the SAW-induced type-II band-edge modulation of the n-doped MoS_2 flake.

Because of the small value of the photon momentum, the wavevector of the SPPs on the graphene layer is mismatched with that of the electromagnetic wave in free space. This leads to a THz emission bottleneck. To bridge this mismatch, microstructures with periodic dielectric gratings were introduced to fold the SPP dispersion back into the center of the Brillouin zone (BZ) in a manner analogous to the translational invariance of a crystal [11,15,16]. The folded SPP dispersion crosses the dispersion of the electron beam within the radiation region formed by the light line, and the momentum of the SPPs and the THz wave is matched. To realize band folding of the SPP dispersion, well-designed periodic dielectric microstructures must be fabricated precisely.

As an alternative to these well-designed microstructures, application of a radio-frequency surface acoustic wave (SAW) field to a piezoelectric semiconductor material provides another way to generate periodic permittivity. Dynamic modulation of the band-edge profile and the charge carrier distributions via application of SAW fields on piezoelectric materials has been performed since the early 1980s [17,18]. When an external SAW field is applied to the surface of a piezoelectric semiconductor, electrons and holes are trapped periodically at separate positions by the SAW-induced piezoelectric potential field. The dielectric responses of these trapped free electrons cause spatially periodic permittivity to occur on the surface of the piezoelectric material. Because of their high-fidelity carrier dynamics, SAW-based modulations have been widely used to modulate the spatiotemporal distributions of charge carriers in a variety of low-dimensional piezoelectric semiconductor systems, including quantum wells [19,20], quantum dots [21,22], nanowires [23,24], and layered transition metal dichalcogenides [24–27]. In addition to the modulations on the charge carrier distributions, the ideal of coupling SPPs into SAW-modulated system also has a long history since 1980s [28]. In

Optics EXPRESS

these studies, the SAW fields were used to generate "dynamic" grating on the metal surfaces [29–31] or graphene layers [32–34] to interact with surface plasmon or light.

In this work, we present a theoretical study of SAW-modulated THz radiation from SPP resonance in a graphene layer that has been excited using a beam of moving electrons. The system is illustrated schematically in Fig. 1(a). In our *gedanken* experiment, the graphene layer is aligned on an n-doped molybdenum disulfide (MoS_2) flake with an odd number of layers that has strong piezoelectricity properties and forms a heterostructure with the graphene layers. The graphene layer and the MoS_2 flake are laid on a quartz substrate with a dielectric constant of $4.2\varepsilon_0$ (where ε_0 is the permittivity of a vacuum). Application of an external SAW field to the MoS_2 flake layer causes the charge carriers of this piezoelectric semiconductor to be periodically separated in space and results in the material having the dielectric response of free electrons with the same period. By summing the dielectric responses of the ions and the SAW-modulated free electrons [35], a periodic permittivity structure is realized dynamically on the MoS_2 flake. In our system, this MoS_2 flake with periodic permittivity acts as a periodic dielectric microstructure to fold the excited graphene SPP dispersion into the center of the BZ and this leads to matching of the momentums.

To give an accurate description on the SAW-modulated THz radiations, we calculate the charge carrier distributions of the MoS_2 flake under the SAW field by self-consistently solving a drift-diffusion model that was coupled with a time-dependent continuity equation and the Poisson equation. The periodic permittivity is then obtained using the Drude model with the calculated charge distributions. The SPP dispersion curves and the power intensity of the THz radiation are calculated thereafter by solving the Maxwell equations with the boundary conditions at the interfaces between regions I, II, and III, as illustrated in Fig. 1(b). The crossing points of the SPP dispersion curve with the electron beam are folded into the cone of the light line around the center of the BZ under the applied SAW field. This results in conservation of the momentum of the SPPs on graphene and the electromagnetic wave in a vacuum, and this leads to THz wave emission. We also show that both the frequency and the intensity of the THz radiation can be tuned by varying the chemical potential of the graphene layer, the doping density of the MoS_2 flake, and the period and wavelength of the external SAW field. Additionally, a maximum conversion efficiency of as much as 0.9 can be obtained for the energy transition from the SPP resonance to THz radiation in free space.

2. Theoretical methods

2.1 Periodically distributed charge and dielectric response under the SAW field

The spatiotemporal distributions of the electrons $n(z,t)$ and the holes $p(z,t)$ on the MoS_2 flake under the applied SAW field can be described using a 1D drift-diffusion model coupled with a time-dependent continuity equation [36,37] as follows:

$$\frac{\partial p(z,t)}{\partial t}=\frac{k_B T}{q}\mu_p\frac{\partial^2 p(z,t)}{\partial z^2}-\mu_p E(z,t)\frac{\partial p(z,t)}{\partial z}-\mu_p p(z,t)\frac{\partial E(z,t)}{\partial z}-R(z,t) \quad (1)$$

$$\frac{\partial n(z,t)}{\partial t}=\frac{k_B T}{q}\mu_n\frac{\partial^2 n(z,t)}{\partial z^2}+\mu_n E(z,t)\frac{\partial n(z,t)}{\partial z}+\mu_n n(z,t)\frac{\partial E(z,t)}{\partial z}-R(z,t) \quad (2)$$

where k_B is the Boltzmann constant, T is the temperature, q is the electron charge, and μ_n and μ_p denote the electron and hole mobilities, respectively. The recombination rate $R(z,t)$ is expressed in the form of $R(z,t)=C_R n(z,t)\,p(z,t)$ using the empirical recombination coefficient C_R. The electronic field $E(z,t)$ used in Eqs. (1) and (2) is the sum

Optics EXPRESS

of the piezoelectric field $E_{SAW}(z,t)$ that is induced by the external SAW field and the built-in field $E_B(z,t)$ that is induced by the spatially unbalanced distribution of the charge carriers. The built-in field can be calculated by solving the Poisson equation

$$\frac{\partial E_B(z,t)}{\partial z} = \frac{q}{\varepsilon}\left[p(z,t) - n(z,t) + N_D\right] \tag{3}$$

with the dielectric permittivity ε and the donor impurity density N_D, while the piezoelectric field caused by the SAW field is written as

$$E_{SAW}(z,t) = A_{SAW}\sin[2\pi\left(\frac{z}{\lambda_{SAW}} - \frac{t}{T_{SAW}}\right)] \tag{4}$$

with the SAW field wavelength λ_{SAW} and period T_{SAW}. The intensity of the piezoelectricity field is described using the parameter A_{SAW}.

When the spatiotemporal charge distributions modulated using the external SAW field are calculated self-consistently by solving the coupled Eqs. (1)–(4) using the parameters given in Table 1, the dielectric response of the free charges $\varepsilon_r(z,t)$ can be calculated approximately using the Drude model [38], given by

$$\varepsilon_r(z,t) = 1 - \frac{n(z,t)q^2}{\varepsilon_0 m\omega_{SAW}^2} \tag{5}$$

with the electron mass m and the SAW field frequency ω_{SAW}. Because of the donor doping of the MoS_2 flake, we only consider the dielectric response of the free electrons in the following. In principle, the mobile charge carriers in the graphene layer lead to an additional dielectric screening on the MoS_2 flake. However, due to the much faster transport speed of the electron beam comparing to the SAW field, the effect of this additional screening can be viewed as a homogeneous reduction of the relative permittivity in MoS_2 flake without breaking the periodic dielectric structures. Screening induced by the electron beam in graphene layer is therefore not taken into account in the periodic dielectric structures [39].

Table 1. Parameters Used in the Model Calculations

Electron mobility	μ_n	215 $cm^2V^{-1}s^{-1}$ [40]
Hole mobility	μ_p	70 $cm^2V^{-1}s^{-1}$ [40]
Dielectric constant of MoS_2	ε_{II}	4.2 ε_0 [41]
Dielectric constant of quartz	ε_{III}	4.2 ε_0
Recombination coefficient	C_R	3 cm^2s^{-1} [42]
Intrinsic semiconductor	n_i	$1.4561\times10^6\,cm^{-2}$

2.2 SPP dispersion and THz radiation with periodic dielectric structure

When an electron beam moves on top of the graphene layer, the electromagnetic fields in the vacuum region, the periodic permittivity region and the substrate (regions I, II and III, respectively, as labeled in Fig. 1) are written as

Optics EXPRESS

$$E_z = \begin{cases} A_1 e^{ik_1(y-d)} & (\mathrm{I}: y > d) \\ \left(A_2 e^{ik_2 y} + A_3 e^{-ik_2(y-d)}\right) & (\mathrm{II}: 0 < y \le d), \\ A_4 e^{-ik_3 y} & (\mathrm{III}: y \le 0) \end{cases} \tag{6}$$

$$H_x = \begin{cases} \dfrac{\omega\varepsilon_0}{k_1} A_1 e^{ik_1(y-d)} & (\mathrm{I}: y > d) \\ \dfrac{\omega\varepsilon_{II}\varepsilon_0}{k_2}\left(A_2 e^{ik_2 y} - A_3 e^{-ik_2(y-d)}\right) & (\mathrm{II}: 0 < y \le d), \\ -\dfrac{\omega\varepsilon_{III}\varepsilon_0}{k_3} A_4 e^{-ik_3 y} & (\mathrm{III}: y \le 0) \end{cases} \tag{7}$$

where $k_1 = \sqrt{k_0^2 - k_z^2}$, $k_2 = \sqrt{\varepsilon_{II} k_0^2 - k_z^2}$, and $k_3 = \sqrt{\varepsilon_{III} k_0^2 - k_z^2}$, where k_0 is the wavevector in a vacuum, k_z is the wavevector of the SPP modes in the *z*-direction, and ε_{II} and ε_{III} are the permittivities of regions II and III, respectively. The electromagnetic field coefficients $A_1 - A_4$ are obtained by solving Eqs. (6) and (7) with the following boundary conditions:

$$E_z^i|_{y=d} + E_z^{\mathrm{I}}|_{y=d} = E_z^{\mathrm{II}}|_{y=d}, \left(H_x^{\mathrm{II}} - H_x^{\mathrm{I}} - H_x^{\mathrm{i}}\right)|_{y=d} = \sigma_g E_z^{\mathrm{II}}|_{y=d} \tag{8}$$

and

$$E_z^{\mathrm{II}}|_{y=0} = E_z^{\mathrm{III}}|_{y=0}, H_x^{\mathrm{II}}|_{y=0} = H_x^{\mathrm{III}}|_{y=0} \tag{9}$$

The electromagnetic field induced by the moving electron beam is then written as [11,15,16]

$$\begin{cases} E_z^i = -\dfrac{qk_c}{2\omega\varepsilon_0} e^{-ik_c(y-b-d)} e^{ik_z z} \\ H_x^i = \dfrac{q}{2} e^{-ik_c(y-b-d)} e^{ik_z z} \end{cases} \tag{10}$$

where $k_c = \sqrt{k_0^2 - k_z^2}$ and $k_z = \omega / v_0$, where the speed of the electron beam is v_0. The electron conductivity of the graphene layer is then calculated using the Drude model as [16,43]

$$\sigma_g = \frac{iq^2 k_B T}{\pi\hbar^2\left(\omega + i\tau^{-1}\right)}\left[\frac{\mu_c}{k_B T} + 2\ln\left(e^{-\frac{\mu_c}{k_B T}} + 1\right)\right] \tag{11}$$

where the tunable chemical potential is μ_c and the electron lifetime is τ.

Using the calculated electromagnetic field amplitude in region III (A_4) with the boundary conditions given in Eqs. (8) and (9), the power intensity of the THz radiation is then calculated as

$$P_z(\omega) = -\frac{1}{2}\mathrm{Re}\left[E_z^{\mathrm{III}} \times H_x^{\mathrm{III}}\right] = \mathrm{Re}\left[\frac{\kappa_3}{2\omega\varepsilon_0\varepsilon_{\mathrm{III}}}|A_4|^2\right] \tag{12}$$

with

Optics EXPRESS

$$A_4 = \frac{\frac{q}{2} e^{ik_c b}\left(1+\frac{k_c}{\kappa_1}\right)\left(M + e^{i\kappa_2 d}\right)}{\left(Me^{i\kappa_2 d}+1\right) - \left(\frac{\sigma_g \kappa_2}{\omega\varepsilon_0\varepsilon_{II}} + \frac{\kappa_2}{\varepsilon_{II}\kappa_1}\right)\left(Me^{i\kappa_2 d}-1\right)} \tag{13}$$

and

$$M = \frac{\varepsilon_{III}\kappa_2 - \varepsilon_{II}\kappa_3}{\varepsilon_{III}\kappa_2 + \varepsilon_{II}\kappa_3} e^{i\kappa_2 d} \tag{14}$$

where κ_i (i = 1, 2 and 3) denotes the equivalent wavevector of k_i when folded into the center of the BZ.

To obtain the dispersion relationship of the SPP resonance, we apply the following boundary conditions along with Eqs. (6) and (7):

$$E_z^{\mathrm{I}}|_{y=d} = E_z^{\mathrm{II}}|_{y=d},\ \left(H_x^{\mathrm{II}} - H_x^{\mathrm{I}}\right)|_{y=d} = \sigma_g E_z^{\mathrm{I}}|_{y=d} \tag{15}$$

and

$$E_z^{\mathrm{II}}|_{y=0} = E_z^{\mathrm{III}}|_{y=0},\ H_x^{\mathrm{II}}|_{y=0} = H_x^{\mathrm{III}}|_{y=0} \tag{16}$$

The SPP dispersion is then given as

$$\frac{\overline{\varepsilon_{II}}\kappa_3 - \varepsilon_{III}\kappa_2}{\overline{\varepsilon_{II}}\kappa_3 + \varepsilon_{III}\kappa_2} e^{2i\kappa_2 d} = \frac{\kappa_1\omega\varepsilon_0\overline{\varepsilon_{II}} + \kappa_1\kappa_2\sigma_g + \kappa_2\omega\varepsilon_0}{\kappa_1\omega\varepsilon_0\overline{\varepsilon_{II}} - \kappa_1\kappa_2\sigma_g - \kappa_2\omega\varepsilon_0} \tag{17}$$

where the averaged permittivity of region II is $\overline{\varepsilon_{II}}$.

3. Results and discussion

3.1 Periodic dielectric structures induced by the SAW field

In Figs. 2(a) and 2(b), we plot the spatial distribution of the electron concentration and the corresponding dielectric response of the MoS_2 flakes when doped with N_D = 1.0 × 10^{10} cm^{-2} (black solid lines), 1.5 × 10^{10} cm^{-2} (red dash-and-dotted lines), and 2.0 × 10^{10} cm^{-2} (blue dashed lines). The amplitude, wavelength, and period of the applied SAW field were set at 8 kV/cm, 2 μm and 2 ns, respectively, in these calculations. Because of the high in-plane carrier mobility of the MoS_2 flake, the electrons and holes arrive at their equilibrium positions quickly, within 0.1 ps after application of the SAW field. The charge carriers are subsequently transported "slowly" along the z direction with the propagation of the SAW. As shown in Fig. 2(a), the electrons are localized within SAW-induced periodic "valleys" of the conduction band minimum (CBM). The dielectric responses of these periodically distributed free electrons lead to periodic permittivity in these spaces, as indicated in Fig. 2(b). Comparison of Figs. 2(a) and 2(b) shows that the "peak" permittivity values correspond to the "valleys" of the electron concentrations and vice versa, as indicated by Eq. (5). Additionally, we find that the dielectric screening effect decreases rapidly as the donor density of the MoS_2 flake increases. A negative permittivity, which corresponds to the dielectric response of the metal, is obtained when the doping density is as high as 2.0 × 10^{10} cm^{-2}.

Optics EXPRESS

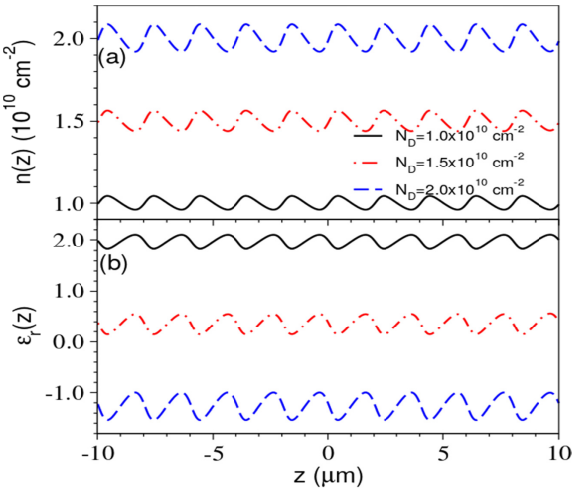

Fig. 2. Spatial distributions of (a) electron concentration and (b) relative permittivity induced by dielectric screening of the free electrons of the MoS_2 flake under a SAW field with period of 2 ns, wavelength of 2 μm, and amplitude of 8 kV/cm. The distributions of the electron concentration and the permittivity when the doping density N_D = 1.0 × 10^{10} cm^{-2}, 1.5 × 10^{10} cm^{-2}, and 2.0 × 10^{10} cm^{-2} are color coded as solid black, dash-and-dotted red, and dashed blue lines, respectively.

Unlike the fabricated microstructures, the spatial distribution and the amplitude of the dielectric response can be tuned dynamically by varying the wavelength and the intensity of the external SAW field. In Figs. 3(a) and 3(b), we plot the calculated $n(z)$ and $\varepsilon_r(z)$ characteristics of a MoS_2 flake after setting a wavelength of 2 μm with intensities of A_{SAW} = 5 and 7 kV/cm (black solid lines and red dash-and-dotted lines), and a wavelength of 3 μm with A_{SAW} = 10 kV/cm (blue dashed lines). In this figure, the period of the applied SAW field is fixed at 2 ns and the MoS_2 flake doping density is set at N_D = 1.2 × 10^{10} cm^{-2}. From Fig. 3, we see that: (i) an external SAW field with intensity of 5 kV/cm causes a fluctuation of the permittivity value of approximately 0.2 ε_0 within a single period, and the modulation increases to 0.4 ε_0 when A_{SAW} reaches 10 kV/cm; (ii) the spatial distribution of the dielectric response varies with the wavelength of the SAW field.

Optics EXPRESS

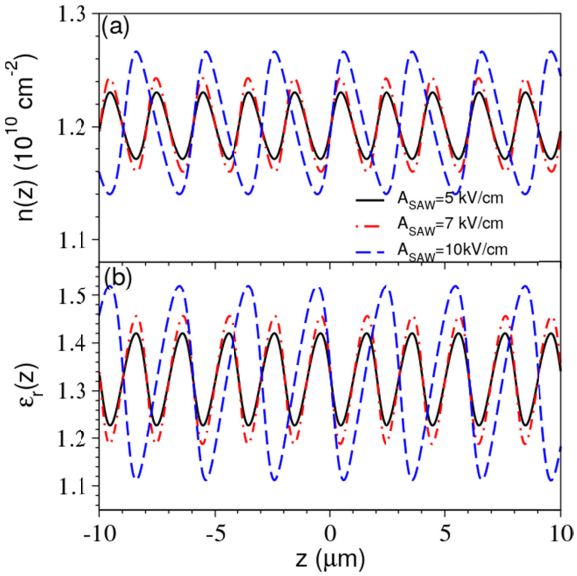

Fig. 3. Spatial distributions of (a) electron concentration and (b) relative permittivity when modulated using external SAW fields. The donor density of the MoS_2 flake $N_D = 1.2 \times 10^{10}$ cm^{-2}. The wavelength of the external SAW field was set at 2 μm with amplitudes of 5 kV/cm (black solid lines) and 7 kV/cm (red dash-and-dotted lines); the wavelength was also set at 3 μm with an amplitude of 10 kV/cm (blue dashed lines). The period of the applied SAW field was 2 ns.

3.2 Dynamic modulation of THz emission via SAW field

When an electron beam moves on top of the graphene layer aligned on the SAW-modulated MoS_2 flake and excites the SPP resonance on the graphene layer, the periodic permittivity structure induced by the SAW field folds the dispersion curves of the SPPs into the center of the BZ. The dispersion curve of the SPPs, the electron beam at a speed of $0.0096\,c$, and the light line in the quartz substrate with permittivity of $4.2\,\varepsilon_0$ are shown in Fig. 4, where the first BZ is highlighted in cyan. The SPP dispersion curve presented in Fig. 4 is calculated by solving Eq. (17) using the chemical potential of the graphene layer $\mu_c = 0.45$ eV and the electron lifetime $\tau = 0.1$ ps. The periodic permittivity is modulated by the SAW field with $\lambda_{SAW} = 2$ μm, $T_{SAW} = 2$ ns, and $A_0 = 7$ kV/cm. Figure 4 shows that the folded SPP dispersion curve crosses the electron beam line near the center of the first BZ and the crossing point is located within the cone of the light line (labeled point A in the figure). Because of the conservation of both energy and momentum, the energies of the graphene SPP oscillations are transformed into THz emissions.

Optics EXPRESS

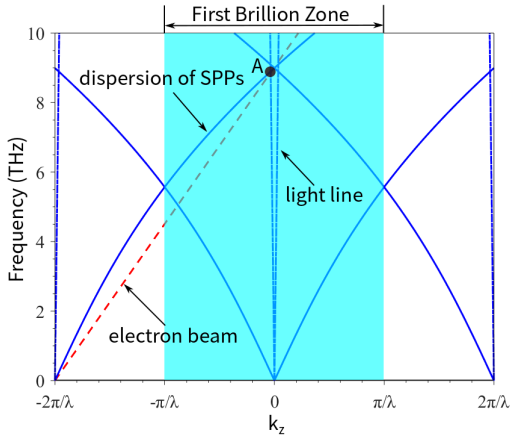

Fig. 4. Dispersion curves of the SPPs (blue solid lines) along with the light line (blue dashed line) and the electron beam, which has a speed of 0.0096 c (red dashed line). The crossing point of the electron beam and the SPP curve in the first BZ (highlighted in cyan) is labeled point A.

As shown in Fig. 4, the radiation frequency is determined by the crossing point of the SPP dispersion curve and the electron beam. To tune this radiation frequency, we adjust the chemical potential of the graphene layer μ_c over the range from 0.35 to 0.55 eV, the MoS_2 flake doping density N_D from 1.0×10^{10} to 1.4×10^{10} cm^{-2}, the SAW field period T_{SAW} from 1.0 to 1.8 ns and the SAW field wavelength λ_{SAW} from 1 to 5μm. The SPP dispersion curves and their crossing points with the electron beam lines that were calculated using these parameters are presented in Figs. 5(a)–5(d). Because the size of the BZ varies with the different wavelengths of the SAW field, the *x*-axis in Fig. 5(d) is labeled with units of $2\pi/\mu m$ rather than $2\pi/\lambda$. Figure 5 shows that the slope of the SPP dispersion curves varies with changes in the chemical potential, the donor density, and the period and wavelength of the SAW field, and this forms a crossing region with the dispersion curve of the electron beam. We labeled this crossing region as the working region of the THz radiation and have highlighted it in green.

In Figs. 6(a) and 6(b), we plotted the modulated THz radiation frequencies that were extracted from the working region by varying the wavelength and period of the SAW field. In this figure, the THz radiation frequencies were calculated using parameter sets of $\mu_c = 0.35$ eV and $N_D = 1.2 \times 10^{10}$ cm^{-2} (black lines), $\mu_c = 0.45$ eV and $N_D = 1.0 \times 10^{10}$ cm^{-2} (red lines), $\mu_c = 0.45$ eV and $N_D = 1.2 \times 10^{10}$ cm^{-2} (green lines), $\mu_c = 0.45$ eV and $N_D = 1.4 \times 10^{10}$ cm^{-2} (blue lines), and $\mu_c = 0.50$ eV and $N_D = 1.2 \times 10^{10}$ cm^{-2} (cyan lines). The period and wavelength of the SAW field were fixed at 2 ns and 2 μm, respectively, in Figs. 6(a) and 6(b) by varying the SAW field propagation velocity. Figure 6(a) shows that the radiation frequencies decrease from approximately 20 THz to a few THz when the SAW field wavelength increases from 0.5 to 5 μm. The red shift in the THz emission is the result of a reduction in the size of the BZ with increasing SAW field wavelength. In contrast to Fig. 6(a), we see a blue shift in THz emission with increasing SAW field period in Fig. 6(b). This blue shift can be understood from the curves in Fig. 5(c), where the slopes of the SPP dispersion curves increase with increasing T_{SAW} and thus shift the working region to a higher frequency range. Additionally, the blue shift in the THz radiation frequency with increases in the chemical potential of the graphene layer and the donor density in the MoS_2 flake can be understood from the curves in Figs. 5(a) and 5(b), respectively.

Optics EXPRESS

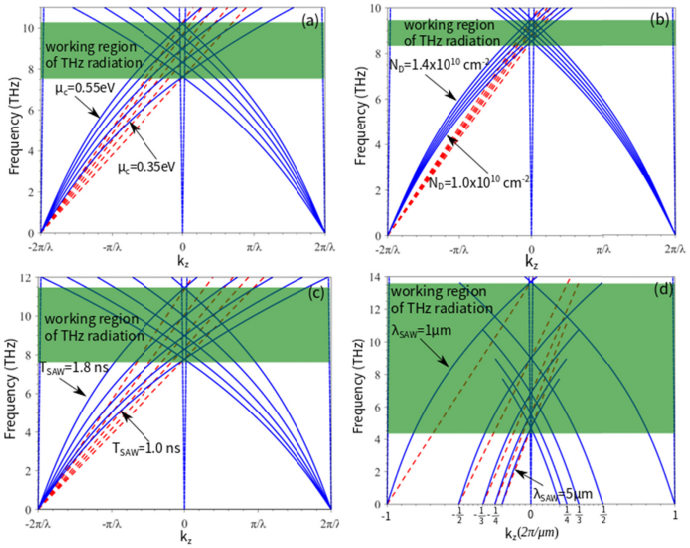

Fig. 5. SPP dispersion curves and their crossing points with the electron beam lines as a result of tuning (a) the chemical potential of the graphene layer, (b) the doping density of the MoS_2 flake, (c) the SAW field period and (d) the SAW field wavelength. The SPP dispersion curves, the electron beam lines and the light lines are shown as blue solid lines, red dashed lines, and blue dashed lines, respectively. The working regions of the THz radiation are highlighted in green.

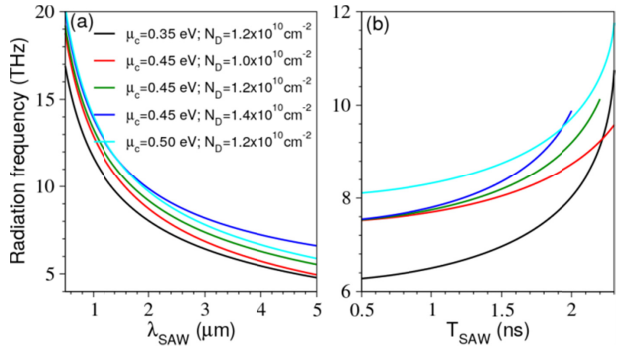

Fig. 6. Frequencies of THz radiation as functions of (a) the wavelength and (b) the period of the applied SAW field. The SAW field period is set at 2.0 ns in (a), while the wavelength is set at 2.0 μm in (b).

In Figs. 7(a) and 7(b), we present the modulations of the THz radiation intensity produced by tuning the wavelength and the period of the SAW field, respectively. The calculations were performed using the same parameters that were used in Fig. 6. Figure 7(a) shows that (i) the THz radiation intensity increases with increasing SAW field wavelength and then decreases after reaching the peak value; (ii) reductions of both the chemical potential of the graphene layer and the MoS_2 flake doping density are required to increase the THz emission intensity; and (iii) a SAW field with a longer wavelength is required to obtain the peak THz radiation intensity value in the case of low chemical potential and low doping density. In Fig. 7(c), we re-plotted the THz radiation intensity curves presented in Fig. 7(a) as a function of radiation frequency using the relationship between the THz frequency and the SAW field wavelength given in Fig. 6(a). Figure 7(c) shows that the radiation intensity decreases with increasing radiation frequency, which is a result of the inverse proportionality between the THz intensity and the radiation frequency indicated by Eq. (12).

Optics EXPRESS

Having considered modulation of the THz radiation via the SAW field wavelength, we now turn to the effect of the period of the SAW field on the THz emission. As Fig. 7(b) shows, the THz radiation intensity increases slowly when the SAW field period is less than 1.5 ns, and arrives at a peak value when T_{SAW} increases to approximately 1.8 ns. When the chemical potential μ_c and the doping density N_D are reduced, a SAW field with a long period is required to obtain the peak THz radiation value. In addition, the peak THz radiation values remain nearly constant for various doping densities and chemical potentials. As indicated by Eq. (5), the permittivity of the free electrons is proportional to the square of the SAW frequency ω_{SAW}^2 and is inversely proportional to the square of the SAW period $T_{SAW}^2 = \left(\frac{2\pi}{\omega_{SAW}}\right)^2$. We therefore linked the SAW field period with the permittivity $\overline{\varepsilon_{II}}$. The maximum THz radiation intensity value is obtained under the condition $\frac{\partial P_z\left(\overline{\varepsilon_{II}}\right)}{\partial \overline{\varepsilon_{II}}}|_{\overline{\varepsilon_{II}}=\varepsilon_{II}^M} = 0$. To obtain the value of ε_{II}^M, a SAW field with a short period is required to balance the effects of the high doping density N_D and the chemical potential μ_c. In Fig. 7(d), we have plotted the THz radiation intensity that was presented in Fig. 7(b) as a function of the radiation frequency by using the relationship between the radiation frequency and the SAW field period given in Fig. 6(b). Interestingly, Fig. 7(d) shows that both the intensity and the frequency of the THz radiation remain nearly constant for the various chemical potentials and doping densities. This behavior can be understood as follows. In systems with fixed chemical potential, the SAW field period changes with the variation of the doping density N_D to keep the value of $\overline{\varepsilon_{II}}$ constant and this leads to the same radiation intensity and frequency indicated by Eqs. (12)–(14) and Eq. (17). For systems with different chemical potentials, a SAW field with a long period is required to balance the reduction of the chemical potential for the peak THz radiation intensity value.

To estimate the efficiency of the conversion of the SPPs into THz radiation, we calculate the conversion efficiency $\eta = \frac{P_z(\omega)}{P_e(\omega)}$ using the power intensity of the THz emission $P_z(\omega)$ and the total energy of the electromagnetic field induced by the electron beam $P_e(\omega)$. The electromagnetic field energy is calculated using the relationship $P_e(\omega) = -\frac{1}{2}\mathrm{Re}\left[E^i \times H^i\right]$. The efficiencies of THz radiation conversion via tuning of the wavelength and the SAW field period are presented in Figs. 8(a) and 8(b), respectively. These conversion efficiencies are calculated using the parameter sets μ_c = 0.35 eV and N_D = 1.2×10^{10} cm^{-2} (black lines), μ_c = 0.45 eV and N_D = 1.0×10^{10} cm^{-2} (red lines), and μ_c = 0.45 eV and N_D = 1.0×10^{12} cm^{-2} (green lines) with a fixed SAW field period T_{SAW} = 2.0 ns and wavelength λ_{SAW} = 2.0 μm in Figs. 8(a) and 8(b). When we compare Figs. 7 and 8, we see the same tuning of both the conversion efficiency and the radiation intensity produced by variation of the wavelength and the period of the SAW field. These results indicate that the large THz radiation intensity values originate from the high efficiency of the energy conversion from the SPP resonance to the THz light. Additionally, the maximum conversion efficiency of as much as 0.9 presented in Fig. 8 indicates the feasibility of THz radiation generation using SAW field-modulated SPP resonance in graphene-MoS_2 devices.

Optics EXPRESS

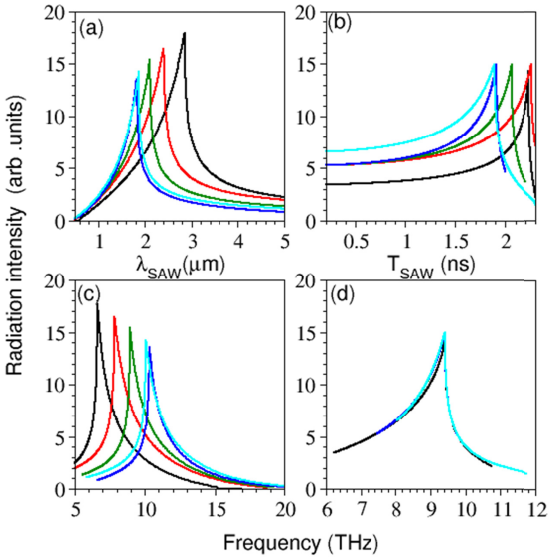

Fig. 7. THz radiation intensity as a function of (a) the wavelength and (b) the period of the applied SAW field. The SAW field period in (a) is 2.0 ns and the SAW field wavelength is 2.0 μm in (b). The radiation intensities presented in (a) and (**b**) are re-plotted as functions of the radiation frequency in (c) and (d), respectively. The chemical potential of the graphene layer and the MoS_2 flake doping density are μ_c = 0.35 eV and N_D = 1.2 × 10^{10} cm^{-2} (black lines), μ_c = 0.45 eV and N_D = 1.0 × 10^{10} cm^{-2} (red lines), μ_c = 0.45 eV and N_D = 1.0 × 10^{12} cm^{-2} (green lines), μ_c = 0.45 eV and N_D = 1.4 × 10^{10} cm^{-2} (blue lines), and μ_c = 0.50 eV and N_D = 1.2 × 10^{10} cm^{-2} (cyan lines).

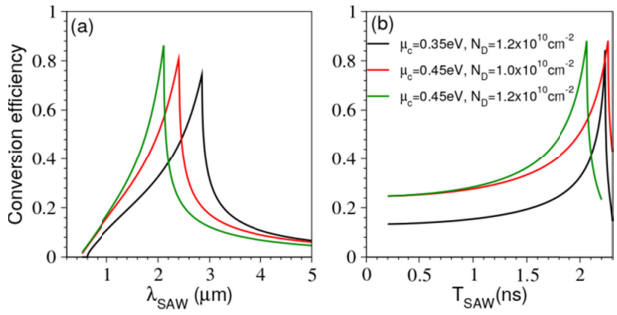

Fig. 8. THz radiation conversion efficiency as functions of (a) the wavelength and (b) the period of the applied SAW field. The SAW field period is 2.0 ns in (a) and the SAW field wavelength is 2.0 μm in (b).

Before concluding this paper, we would like to emphasis that the charge carrier transfer between the graphene layer and the semiconducting MoS_2 layer changes both the chemical potential and the free charge carrier density of graphene and MoS_2 layers as formatting a van der Waals heterostructure [44–46]. Although two parameters μ_c and N_D are used to describe the chemical potential in the graphene layer and free charge carrier density in the MoS_2 flake in our model calculation, such charge carrier transfer effect cannot be simply neglected in real systems.

4. Conclusion

In summary, we have theoretically studied the THz radiation that is excited by a moving electron beam on top of a graphene layer aligned on an *n*-doped MoS_2 flake under modulation

Optics EXPRESS

by an external SAW field. The spatial periodic permittivity of the MoS_2 flake is obtained using the Drude model with self-consistently calculated charge carrier distributions that are modulated using the SAW field. By folding the crossing point of the SPP dispersion curve with the electron beam line in the center of the BZ to converge the momentum of the SPPs and the electron beam within the cone of the light line, the transformation of the SPPs into THz radiation is achieved. The frequency and intensity of the THz radiation can be tuned by varying the MoS_2 flake doping density, the chemical potential of the graphene layer, and the period and wavelength of the applied SAW field. Based on our calculations, a maximum conversion efficiency of as much as 0.9 is obtained for the energy transformation from the SPP resonance to the THz emission. Our results suggest an exciting opportunity for development of dynamically tunable THz sources based on SPPs in a graphene layer.

Funding

National Natural Science Foundation of China (11774243, 11404224, 11774246, 11474206); Youth Innovative Research Team of Capital Normal University (008/19530050146); Beijing Youth Top-Notch Talent Training Plan (CIT&TCD 201504080); Beijing Nova Program (Z161100004916100); Capacity Building for Science & Technology Innovation - Fundamental Scientific Research Funds (008/19530050170, 008/19530050180, 008/18530500186, 025185305000/142); Scientific Research Base Development Program of the Beijing Municipal Commission of Education.

Acknowledgments

We thank David MacDonald, MSc, from Liwen Bianji, Edanz Editing China (www.liwenbianji.cn/ac), for editing the English text of a draft of this manuscript.

References

1. M. Tonouchi, "Cutting-edge terahertz technology," Nat. Photonics **1**(2), 97–105 (2007).
2. J. Hebling, M. C. Hoffmann, H. Y. Hwang, K. L. Yeh, and K. A. Nelson, "Observation of nonequilibrium carrier distribution in Ge, Si, and GaAs by terahertz pump–terahertz probe measurements," Phys. Rev. B Condens. Matter Mater. Phys. **81**(3), 035201 (2010).
3. K. Krügener, M. Schwerdtfeger, S. F. Busch, A. Soltani, E. Castro-Camus, M. Koch, and W. Viöl, "Terahertz meets sculptural and architectural art: Evaluation and conservation of stone objects with T-ray technology," Sci. Rep. **5**(1), 14842 (2015).
4. H. Zhong, A. Redo-Sanchez, and X.-C. Zhang, "Identification and classification of chemicals using terahertz reflective spectroscopic focal-plane imaging system," Opt. Express **14**(20), 9130–9141 (2006).
5. E. Grossman, C. Dietlein, J. Ala-Laurinaho, M. Leivo, L. Gronberg, M. Gronholm, P. Lappalainen, A. Rautiainen, A. Tamminen, and A. Luukanen, "Passive terahertz camera for standoff security screening," Appl. Opt. **49**(19), E106–E120 (2010).
6. Ch. Fattinger and D. Grischkowsky, "Terahertz beams," Appl. Phys. Lett. **54**(6), 490–492 (1989).
7. A. Rice, Y. Jin, X. F. Ma, X.-C. Zhang, D. Bliss, J. Larkin, and M. Alexander, "Terahertz optical rectification from 〈 110〉 zinc- blende crystals," Appl. Phys. Lett. **64**(11), 1324–1326 (1994).
8. D. J. Cook and R. M. Hochstrasser, "Intense terahertz pulses by four-wave rectification in air," Opt. Lett. **25**(16), 1210–1212 (2000).
9. S. Barbieri, M. Ravaro, P. Gellie, G. Santarelli, C. Manquest, C. Sirtori, S. P. Khanna, E. H. Linfield, and A. G. Davies, "Coherent sampling of active mode-locked terahertz quantum cascade lasers and frequency synthesis," Nat. Photonics **5**(5), 306–313 (2011).
10. A. M. Cook, R. Tikhoplav, S. Y. Tochitsky, G. Travish, O. B. Williams, and J. B. Rosenzweig, "Observation of narrow-band terahertz coherent Cherenkov radiation from a cylindrical dielectric-lined waveguide," Phys. Rev. Lett. **103**(9), 095003 (2009).
11. T. Zhan, D. Han, X. Hu, X. Liu, S. Chui, and J. Zi, "Tunable terahertz radiation from graphene induced by moving electrons," Phys. Rev. B Condens. Matter Mater. Phys. **89**(24), 245434 (2014).
12. B. Wunsch, T. Stauber, F. Sols, and F. Guinea, "Dynamical polarization of graphene at finite doping," New J. Phys. **8**(12), 318 (2006).
13. E. H. Hwang and S. Das Sarma, "Dielectric function, screening, and plasmons in two-dimensional graphene," Phys. Rev. B Condens. Matter Mater. Phys. **75**(20), 205418 (2007).
14. A. N. Grigorenko, M. Polini, and K. S. Novoselov, "Graphene plasmonics," Nat. Photonics **6**(11), 749–758 (2012).

Optics EXPRESS

15. S. Liu, C. Zhang, M. Hu, X. Chen, P. Zhang, S. Gong, T. Zhao, and R. Zhong, "Coherent and tunable terahertz radiation from graphene surface plasmon polaritons excited by an electron beam," Appl. Phys. Lett. **104**(20), 201104 (2014).
16. T. Zhao, M. Hu, R. Zhong, S. Gong, C. Zhang, and S. Liu, "Cherenkov terahertz radiation from graphene surface plasmon polaritons excited by an electron beam," Appl. Phys. Lett. **110**(23), 231102 (2017).
17. M. J. Hoskins, H. Morkoc, and B. J. Hunsinger, "Charge transport by surface acoustic waves in GaAs," Appl. Phys. Lett. **41**(4), 332–334 (1982).
18. A. Wixforth, J. P. Kotthaus, and G. Weimann, "Quantum oscillations in the surface-acoustic-wave attenuation caused by a two-dimensional electron system," Phys. Rev. Lett. **56**(19), 2104–2106 (1986).
19. C. Rocke, S. Zimmermann, A. Wixforth, J. P. Kotthaus, G. Böhm, and G. Weimann, "Acoustically driven storage of light in a quantum well," Phys. Rev. Lett. **78**(21), 4099–4102 (1997).
20. A. García-Cristóbal, A. Cantarero, F. Alsina, and P. V. Santos, "Spatiotemporal carrier dynamics in quantum wells under surface acoustic waves," Phys. Rev. B Condens. Matter Mater. Phys. **69**(20), 205301 (2004).
21. C. Bödefeld, J. Ebbecke, J. Toivonen, M. Sopanen, H. Lipsanen, and A. Wixforth, "Experimental investigation towards a periodically pumped single-photon source," Phys. Rev. B Condens. Matter Mater. Phys. **74**(3), 035407 (2006).
22. F. J. R. Schülein, K. Müller, M. Bichler, G. Koblmüller, J. J. Finley, A. Wixforth, and H. J. Krenner, "Acoustically regulated carrier injection into a single optically active quantum dot," Phys. Rev. B Condens. Matter Mater. Phys. **88**(8), 085307 (2013).
23. M. Weiss, J. B. Kinzel, F. J. R. Schülein, M. Heigl, D. Rudolph, S. Morkötter, M. Döblinger, M. Bichler, G. Abstreiter, J. J. Finley, G. Koblmüller, A. Wixforth, and H. J. Krenner, "Dynamic acoustic control of individual optically active quantum dot-like emission centers in heterostructure nanowires," Nano Lett. **14**(5), 2256–2264 (2014).
24. J. B. Kinzel, F. J. R. Schülein, M. Weiß, L. Janker, D. D. Bühler, M. Heigl, D. Rudolph, S. Morkötter, M. Döblinger, M. Bichler, G. Abstreiter, J. J. Finley, A. Wixforth, G. Koblmüller, and H. J. Krenner, "The native material limit of electron and hole mobilities in semiconductor nanowires," ACS Nano **10**(5), 4942–4953 (2016).
25. E. Preciado, F. J. R. Schülein, A. E. Nguyen, D. Barroso, M. Isarraraz, G. von Son, I.-H. Lu, W. Michailow, B. Möller, V. Klee, J. Mann, A. Wixforth, L. Bartels, and H. J. Krenner, "Scalable fabrication of a hybrid field-effect and acousto-electric device by direct growth of monolayer MoS_2/$LiNbO_3$," Nat. Commun. **6**(1), 8593 (2015).
26. A. R. Rezk, B. Carey, A. F. Chrimes, D. W. M. Lau, B. C. Gibson, C. Zheng, M. S. Fuhrer, L. Y. Yeo, and K. Kalantar-Zadeh, "Acoustically-driven trion and exciton modulation in piezoelectric two-dimensional MoS_2," Nano Lett. **16**(2), 849–855 (2016).
27. T. Huang, P. Han, X. Wang, J. Ye, W. Sun, S. Feng, and Y. Zhang, "Theoretical study on dynamic acoustic modulation of free carriers, excitons, and trions in 2D MoS_2 flake," J. Phys. D Appl. Phys. **50**(11), 114005 (2017).
28. A. V. Chaplik and M. V. Krasheninnikov, "Two-dimensional plasmons (2DP) and acoustic waves in crystals," Surf. Sci. **98**(1-3), 533–552 (1980).
29. X. Sun, S. Shiokawa, and Y. Matsui, "Interactions of surface plasmons with surface acoustic waves and the study of the properties of Ag films," J. Appl. Phys. **69**(1), 362–366 (1991).
30. C. Ruppert, J. Neumann, J. B. Kinzel, H. J. Krenner, A. Wixforth, and M. Betz, "Surface acoustic wave mediated coupling of free-space radiation into surface plasmon polaritons on plain metal films," Phys. Rev. B Condens. Matter Mater. Phys. **82**(8), 081416 (2010).
31. C. Ruppert, F. Förster, A. Zrenner, J. B. Kinzel, A. Wixforth, H. J. Krenner, and M. Betz, "Radio frequency electromechanical control over a surface plasmon polariton coupler," ACS Photonics **1**(2), 91–95 (2014).
32. M. Farhat, S. Guenneau, and H. Bağcı, "Exciting graphene surface plasmon polaritons through light and sound interplay," Phys. Rev. Lett. **111**(23), 237404 (2013).
33. J. Schiefele, J. Pedrós, F. Sols, F. Calle, and F. Guinea, "Coupling light into graphene plasmons through surface acoustic waves," Phys. Rev. Lett. **111**(23), 237405 (2013).
34. R. Fandan, J. Pedrós, J. Schiefele, A. Boscá, J. Martínez, and F. Calle, "Acoustically-driven surface and hyperbolic plasmon-phonon polaritons in graphene/h-BN heterostructures on piezoelectric substrate," J. Phys. D Appl. Phys. **51**(20), 204004 (2018).
35. N. Tzoar and C. Zhang, "High-frequency conductivity of superlattices with electron-phonon coupling," Phys. Rev. B Condens. Matter **35**(14), 7596–7603 (1987).
36. S. M. Sez, *Physics of Semiconductor Devices* (Wiley, 1981).
37. D. A. Neamen, *Semiconductor Physics and Devices Basic Principles* 3rd edn (McGraw-Hill, 2003).
38. N. W. Ashcroft and N. D. Mermin, *Solid State Physics* (Thomson Learning Asia Pte Ltd., 1976).
39. P. V. Santosa, T. Schumann, M. H. Oliveira, Jr., J. M. J. Lopes, and H. Riechert, "Acousto-electric transport in epitaxial monolayer graphene on SiC," Appl. Phys. Lett. **102**(22), 221907 (2013).
40. B. Radisavljevic, A. Radenovic, J. Brivio, V. Giacometti, and A. Kis, "Single-layer MoS_2 transistors," Nat. Nanotechnol. **6**(3), 147–150 (2011).
41. S. Cha, J. H. Sung, S. Sim, J. Park, H. Heo, M.-H. Jo, and H. Choi, "1s-intraexcitonic dynamics in monolayer MoS_2 probed by ultrafast mid-infrared spectroscopy," Nat. Commun. **7**(1), 10768 (2016).
42. O. Salehzadeh, N. H. Tran, X. Liu, I. Shih, and Z. Mi, "Exciton kinetics, quantum efficiency, and efficiency droop of monolayer MoS□ light-emitting devices," Nano Lett. **14**(7), 4125–4130 (2014).
43. A. H. Castro Neto, F. Guinea, N. Peres, K. Novoselov, and A. Geim, "The electronic properties of graphene," Rev. Mod. Phys. **81**(1), 109–162 (2009).

Optics EXPRESS

44. W. J. Yu, Y. Liu, H. Zhou, A. Yin, Z. Li, Y. Huang, and X. Duan, "Highly efficient gate-tunable photocurrent generation in vertical heterostructures of layered materials," Nat. Nanotechnol. **8**(12), 952–958 (2013).
45. H. C. Diaz, J. Avila, C. Chen, R. Addou, M. C. Asensio, and M. Batzill, "Direct observation of interlayer hybridization and Dirac relativistic carriers in graphene/MoS□ van der Waals heterostructures," Nano Lett. **15**(2), 1135–1140 (2015).
46. C.-J. Shih, Q. H. Wang, Y. Son, Z. Jin, D. Blankschtein, and M. S. Strano, "Tuning on-off current ratio and field-effect mobility in a MoS(2)-graphene heterostructure via Schottky barrier modulation," ACS Nano **8**(6), 5790–5798 (2014).